BEILSTEIN JOURNAL OF NANOTECHNOLOGY

Ultrasharp gold nanobipyramids: synthetic shape-purity control and SERS-sensitive detection of malachite green

Quang Duy Nguyen‡[1,2], Chau-A Thi Ho‡[1,2], Lo Nu Hoang Tien[3,4], Dohoon Lee[5], Thi Thanh Nguyen Ho[6], Le Vinh Phong[2,7], Vu Thi Hanh Thu[2,7], Hai Son Truong-Lam[1,2], Khuong Quoc Vo*[1,2] and Sy Van Vu*[1,2]

Full Research Paper

Open Access

Address:
[1]Faculty of Chemistry, Ho Chi Minh City University of Science, Vietnam National University, Ho Chi Minh City, 227 Nguyen Van Cu Street, Cho Quan Ward, Ho Chi Minh City 70000, Vietnam, [2]Vietnam National University, Ho Chi Minh City, Vietnam, [3]College of Engineering and Computer Science, VinUniversity, Da-Ton, Gia-Lam, Hanoi 100000, Vietnam, [4]Center for Materials Innovation & Technology, VinUniversity, Da-Ton, Gia-Lam, Hanoi 100000, Vietnam, [5]Research Institute of Clean Manufacturing System, Korea Institute of Industrial Technology (KITECH), 89 Yangdaegiro-gil, Ipjang-myeon, Cheonan 31056, South Korea, [6]Graduate School of Advanced Science and Engineering, Hiroshima University, 1-4-1 Kagamiyama, Higashihiroshima, Hiroshima 739-8527, Japan and [7]Faculty of Physics and Physics Engineering, Ho Chi Minh City University of Science, Vietnam National University, Ho Chi Minh City, 227 Nguyen Van Cu Street, Cho Quan Ward, Ho Chi Minh City 70000, Vietnam

Email:
Khuong Quoc Vo* - vqkhuong@hcmus.edu.vn;
Sy Van Vu* - vuvansy0901@gmail.com

* Corresponding author ‡ Equal contributors

Keywords:
gold nanobipyramids; malachite green; SERS nanosubstrates; shape-purity control

Beilstein J. Nanotechnol. **2026,** *17,* 1663–1681.
https://doi.org/10.3762/bjnano.17.115

Received: 13 August 2026
Accepted: 13 November 2026
Published: 26 November 2026

This article is part of the thematic issue "Innovative nanomaterials for next-generation bio- and chemosensing".

Guest Editor: T.-D. Nguyen

© 2026 Nguyen et al.; licensee Beilstein-Institut.
License and terms: see end of document.

Abstract

Gold nanobipyramids (AuBPs) are particularly attractive because of their sharp tips and strong longitudinal localized surface plasmon resonance. However, the practical application of AuBPs remains hindered by the difficulty of producing high-purity, ultrasharp bipyramidal structures because the formation of penta-twinned seeds is difficult to control. Herein, we report a novel seed-mediated strategy for morphology control with significantly improved shape purity (approximately 76%) by systematically regulating seed evolution and the growth process. The effects of thermal annealing, seed aging time, surfactant chemistry, silver ions, and growth parameters on penta-twinned seed formation and anisotropic crystal growth were also systematically investigated. AuBPs with a maximum aspect ratio of 2.8 and a longitudinal surface plasmon resonance centered at 780 nm were successfully obtained. Structural characterization confirmed the formation of highly crystalline bipyramidal nanoparticles with well-defined twin

boundaries and ultrasharp tips. The AuBPs exhibited remarkable surface-enhanced Raman scattering (SERS) activity toward malachite green (MG) with a limit of detection of 10^{-9} M, an enhancement factor of 3.9×10^6, and excellent signal repeatability with a relative standard deviation of only 8.34%. The SERS signal of MG was not significantly affected by coexisting alkali and alkaline earth metal ions such as Na^+, Ca^{2+}, and Mg^{2+}. Finite-difference time-domain simulations further revealed that the intense electromagnetic fields were predominantly localized at the bipyramids' sharp tips. This work provides high-quality gold nanobipyramids for highly sensitive, reproducible SERS platforms for environmental nanophotonic applications.

Introduction

Surface-enhanced Raman scattering (SERS) has emerged as one of the most powerful spectroscopic techniques for ultrasensitive molecular analysis owing to its unique combination of fingerprint specificity, rapid response, and exceptional detection sensitivity [1,2]. By exploiting localized surface plasmon resonance (LSPR) in noble metal nanostructures [3], SERS dramatically amplifies the inherently weak Raman scattering signals of analyte molecules, enabling detection down to trace concentrations and even the single-molecule level under favorable conditions [4]. Owing to these remarkable characteristics, SERS has attracted tremendous attention in environmental monitoring [5], food safety [6], biomedical diagnostics [7], forensic science [8], and chemical sensing [9]. The analytical performance of SERS is fundamentally governed by the design of plasmonic substrates, whose morphology, composition, crystallinity, and surface architecture directly determine electromagnetic field enhancement and signal reproducibility [10,11]. Among the various plasmonic materials explored for SERS, gold nanostructures have attracted considerable attention due to their excellent chemical stability [12], resistance to oxidation [13], and outstanding biocompatibility [14]. Unlike spherical nanoparticles, anisotropic gold nanostructures possess morphology-dependent optical properties that can be precisely engineered by controlling particle geometry [15]. Gold nanorods, nanostars, nanotriangles, nanocubes, and nanobipyramids have therefore been extensively explored as advanced plasmonic substrates because their anisotropic geometries support multiple plasmon resonance modes and generate substantially stronger electromagnetic enhancement than isotropic nanoparticles [15]. In particular, localized electromagnetic fields are predominantly concentrated in high-curvature regions, such as edges, corners, and sharp tips, through the well-known lightning-rod effect [16], resulting in a remarkable enhancement of Raman signals.

Among these anisotropic nanostructures, gold nanobipyramids (AuBPs) are particularly attractive owing to their unique pentagonal bipyramidal geometry terminated by two atomically sharp tips. Compared with gold nanospheres and conventional nanorods, AuBPs exhibit narrower LSPR bands, larger absorption and scattering cross sections, stronger electric field confinement, and superior refractive index sensitivity [17,18]. Their highly symmetric geometry also provides more homogeneous plasmonic responses, making AuBPs promising candidates for reproducible SERS substrates, plasmonic biosensors, photothermal therapy, photocatalysis, and optical imaging [19,20]. Numerous theoretical and experimental studies have demonstrated that the ultrasharp tips of AuBPs produce significantly stronger electromagnetic hot spots than other anisotropic gold nanostructures, resulting in remarkable Raman enhancement and improved sensing sensitivity [21,22]. Despite these advantages, the controlled synthesis of high-quality AuBPs remains a considerable challenge. Most AuBPs are synthesized through seed-mediated growth, in which the final particle morphology is highly dependent on the crystallographic structure of the initial gold seeds and the kinetics of anisotropic crystal growth. In particular, the formation of penta-twinned seeds plays a decisive role because these multiple twinned structures provide the crystallographic framework required for bipyramidal development [23]. However, penta-twinned seeds generally coexist with single-crystalline or multiply faceted particles, resulting in low shape purity and a significant proportion of undesired by-products such as nanospheres, truncated bipyramids, and irregular nanoparticles. Furthermore, subtle variations in synthetic parameters, including seed aging conditions, annealing temperature, surfactant composition, halide ions, silver ions, acidity, and reduction kinetics, can substantially alter crystal growth pathways and ultimately influence particle morphology, optical properties, and SERS performance. Consequently, achieving highly reproducible synthesis of monodisperse AuBPs with high shape purity remains an important challenge. Previous studies have proposed various strategies to improve AuBP synthesis by optimizing surfactants, adjusting precursor concentrations, or introducing thermal treatment during seed preparation [17,24]. Nevertheless, the individual and cooperative roles of thermal annealing, seed evolution, citrate stabilization, halide chemistry, and silver-assisted anisotropic growth have not yet been systematically clarified [23,25,26]. In particular, a comprehensive understanding of how these parameters regulate the formation of penta-twinned seeds and subsequently determine the morphological evolution toward bipyramidal nanoparticles remains limited. Establishing

such structure–growth relationships is essential not only for improving synthetic reproducibility but also for rationally engineering plasmonic nanostructures with optimized optical properties for SERS applications [24,26].

Malachite green (MG) is a synthetic triphenylmethane dye that has been extensively used in aquaculture because of its broad-spectrum antifungal and antiparasitic activities [27,28]. However, its persistence, bioaccumulation, and potential carcinogenicity have led to strict regulations or complete prohibition in many countries [29,30]. Even trace concentrations of MG remaining in aquatic products or environmental water may pose significant risks to both ecosystems and human health [31]. Conventional analytical techniques, including high-performance liquid chromatography, liquid chromatography–mass spectrometry, and electrochemical analysis, provide high analytical accuracy but generally require sophisticated instrumentation, complicated sample pretreatment, and time-consuming procedures [32,33]. Consequently, developing rapid, highly sensitive, and reproducible SERS substrates capable of detecting trace levels of MG remains highly desirable for environmental and food safety monitoring.

In this work, we report a highly controllable seed-mediated strategy for synthesizing gold nanobipyramids with significantly improved shape purity by systematically regulating seed formation and anisotropic crystal growth. The effects of thermal annealing temperature, annealing duration, surfactant chemistry, and growth parameters on penta-twinned seed evolution and AuBP formation were comprehensively investigated to elucidate the underlying growth mechanism. The resulting AuBPs exhibited highly uniform morphology, well-defined longitudinal plasmon resonance, and excellent crystallinity with ultrasharp tips that efficiently generated localized electromagnetic hot spots. Their SERS performance was evaluated using malachite green as a model analyte, demonstrating highly sensitive detection together with excellent signal reproducibility. Finite-difference time-domain (FDTD) simulations were further performed to correlate the electromagnetic field distribution with the experimentally observed Raman enhancement.

Experimental

Chemicals and materials

Hexadecyltrimethylammonium bromide (CTAB, 99.0%) was purchased from HIMEDIA (Mumbai, India). Hexadecyltrimethylammonium chloride (CTAC, 97.0%) and ciprofloxacin ($C_{17}H_{18}FN_3O_3$, 97.0%) were purchased from Macklin (China). Sodium borohydride ($NaBH_4$, 99.9%), L-ascorbic acid ($C_6H_8O_6$, 99.0%), and hydrochloric acid (HCl, ACS reagent, 37%) were obtained from Sigma-Aldrich (Darmstadt, Germany). Silver nitrate ($AgNO_3$, 99.9%), gold(III) chloride hydrate ($HAuCl_4{\cdot}4H_2O$, 99.5%), and citric acid ($C_6H_8O_7$, 99.9%) were obtained from Sinopharm Chemical Reagent Co., Ltd. (Beijing, China). Malachite green ($C_{23}H_{25}ClN_2$), rhodamine 6G ($C_{28}H_{31}ClN_2O_3$), methylene blue ($C_{16}H_{18}ClN_3S$), 4-mercaptobenzoic acid (HSC_6H_4COOH), 4-aminothiophenol (C_6H_7NS), $AlCl_3$, $NH_4H_2PO_4$, $CaCl_2$, $FeCl_3$, $MgSO_4$, $NaNO_3$ ≥ 99.9% were purchased from Xilong (China).

All chemicals were of analytical grade and were used without any further purification. All experimental solutions were prepared with distilled water. Before synthesizing nanoparticles, glassware and stirring bars were washed with aqua regia (HCl/HNO_3, 3:1 molar ratio) and thoroughly rinsed with DI water.

Synthesis of gold nanobipyramid

This synthesis procedure is based on the method proposed by Sánchez-Iglesias et al. [25] with some adjustments. Penta-twinned seed preparation stage: 3.75 mL of distilled water, 5.0 mL of 0.1 M CTAC, 1.0 mL of 50 mM citric acid, and 0.25 mL of 10 mM $HAuCl_4$ were added to a 20 mL vial, followed by the rapid addition of 0.25 mL of 25 mM $NaBH_4$ (fresh and cooled below 5 °C) under vigorous stirring at room temperature for 2 min. The color of the colloidal solution changed from light yellow to brown. The mixture was then sealed, placed in a water bath at 80 °C, and stirred at 300 rpm for 2 h. The resulting gold seed solution turned reddish-pink. The seed solution was then stored at room temperature and remained stable for a month. Gold nanobipyramid growth stage: The growth solution consisted of 10 mL of 0.1 M CTAB, 0.5 mL of 0.01 M $HAuCl_4$, 0.1 mL of 0.01 M $AgNO_3$, 0.2 mL of 1 M HCl, and 0.08 mL of 0.1 M L-ascorbic acid (AA). Subsequently, a defined volume of the seed solution (100–750 µL) was rapidly added to the growth solution. The solution was gently stirred at 500 rpm and maintained at 30 °C for 2 h. The colloidal solution was centrifuged at 8000 rpm at 30 °C for 10 min, and the precipitate was washed twice with distilled water. The product was then redispersed in 1 mL of 1 mM CTAB and used for subsequent stages.

Preparation of SERS substrates

The malachite green (MG) stock solution was prepared at a concentration of 10^{-2} M before diluting with distilled water to lower concentrations of 10^{-5}, $10^{-5.5}$, 10^{-6}, $10^{-6.5}$, 10^{-7}, $10^{-7.5}$, 10^{-8}, $10^{-8.5}$, and 10^{-9} M. The prepared 1 × 1 cm^2 slides were surface-cleaned by successively soaking in acetone and ethanol, then rinsed with DI water before use. The AuBPs material was thoroughly centrifuged to remove residual surfactants, then dispersed in distilled water before application. 25 µL of the AuBPs colloid solution was applied to a clean slide and allowed to dry at room temperature. Next, 25 µL of the MG solution at

the investigated concentration was applied to the SERS substrate and allowed to evaporate completely at room temperature.

Characterization

UV–vis spectra were obtained using a V-670 UV–vis–NIR spectrophotometer (JASCO, Japan). The samples were measured at room temperature (25–30 °C) with a scanning rate of 400 nm·min^{-1} between 300 and 850 nm, using 1.0 cm quartz cuvettes. The morphology of AuBPs was studied through scanning electron microscopy (SEM) on a JEOL JSM-7600F microscope (Jeol Ltd., Japan). The elemental composition of the AuBPs' surface was also determined using energy-dispersive X-ray spectroscopy (EDS) (Oxford Instruments 50 mm^2 X-max, UK; and Gatan mono, UK). The crystalline structure information of nanoparticles was obtained by X-ray diffraction (XRD) using a D8 Advance Bruker (Germany) with Cu Kα radiation in the 2θ range from 35° to 80° (40 kV, 40 mA). High-resolution transmission electron microscopy (HRTEM) was used to characterize the crystal structure of single particles using an FEI Tecnai G2 F20 (USA) at an accelerating voltage of 200 kV. The lattice parameter and crystalline structure were analyzed using selected-area electron diffraction (SAED) on a JEOL-2100 (Jeol Ltd., Japan). The surface composition of the AuBPs sample was characterized using an X-ray photoelectron spectrometer (Thermo Scientific, USA) equipped with a monochromatic Al Kα X-ray source operating at 1486.7 eV, calibrated with the C 1s binding energy at 284.8 eV.

SERS measurement

Raman spectroscopy of the samples was recorded using the XploRa PLUS confocal Raman Microscope (Horiba France SAS, Longjumeau, France). The excitation wavelength was 638 nm (532 and 785 nm were used only for wavelength selection, Supporting Information File 1, Figure S8), with a 50× objective. The samples were analyzed with 10% of 50 mW laser power and 15 s of exposure time, and the obtained Raman data were processed with the LabSpec 6 Software suite (Horiba, France). Baseline correction, despiking, and denoising were applied to process the raw spectra.

FDTD simulation

The electric field distributions of gold nanobipyramids were simulated by using the 3D finite-difference time-domain (FDTD) method (Lumerical Solutions, Inc.). The geometric models of AuBPs were created using orientation-dependent FESEM images. The gold properties were chosen from the software database, based on Johnson and Christy [34]. A 1 nm mesh size, a conformal variant, one mesh refinement, and a perfectly matched layer were used. The refractive index of the simulation region was set to 1 for air and 1.33 for water. A total-field scattered-field source at the wavelengths of the Raman lasers used in the SERS experiments was employed as the excitation source.

Results and Discussion

Synthesis of gold nanobipyramids

Effects of seed generation conditions

Seed aging: To evaluate the impact of generation temperature, the penta-twinned nanoseeds were synthesized and observed over 120 min at different annealing temperatures (30, 50, and 80 °C). These seed samples were grown at the second stage to observe the efficient formation of AuBPs. The UV–vis spectra of the twinned seeds are shown in Figure 1a; higher annealing temperatures increase the absorption band intensity. The seeds aged at 30 °C for 120 min appeared brown (with no significant change from the initial preparation), and the characteristic plasmon peak in the 500–600 nm range was missing. This suggests that the formed clusters have an average diameter of no more than 3 nm [23,35,36]. Increasing the temperature from 50 to 80 °C causes a color change from brown to red, indicating an increase in particle size. The UV–vis spectrum of the seed sample at 50 °C shows only a shoulder in the characteristic SPR region, whereas the sample at 80 °C exhibits a distinct absorption peak at about 508 nm. Providing heat to the system causes the gold atoms to keep depositing and rearranging, increasing the size of the clusters and potentially leading to the formation of twin defects.

The heat-treated seeds were used to synthesize AuBPs under the same conditions. The UV–vis spectra of the growth solution (Figure 1b) show two surface plasmon resonance peaks appearing at 500–600 and 700–800 nm, corresponding to transverse surface plasmon resonance (t-SPR) and longitudinal surface plasmon resonance (l-SPR), respectively [22,37]. Only a slight wavelength shift was observed for the maximum absorption band at ≈530 nm, but the signal region became wider in the t-SPR region. The t-SPR band showed only a slight red shift from 524 nm at 30 °C to 534 nm at 80 °C (Supporting Information File 1, Table S1). Because the t-SPR of AuBPs overlaps with the dipolar plasmon band of quasi-spherical and polyhedral by-products in this region, this small shift and band broadening could be attributed to the larger transverse dimension of AuBPs grown from well-developed penta-twinned seeds, along with the contribution of the remaining isotropic by-products [24,37]. Studies have shown that a higher intensity of the t-SPR peak indicates isotropic by-products as impurities in the sample [17,24,26]. Meanwhile, a red shift from 701 to 780 nm was observed in the l-SPR region. Furthermore, the absorbance intensity ratio [l-SPR]/[t-SPR] also increased with increasing annealing temperature, from ≈0.4 at 30 °C to ≈2.1 at 50 °C and ≈5.2 at 80 °C. The UV–vis results were significantly reinforced by the morphological characteristics observed using SEM

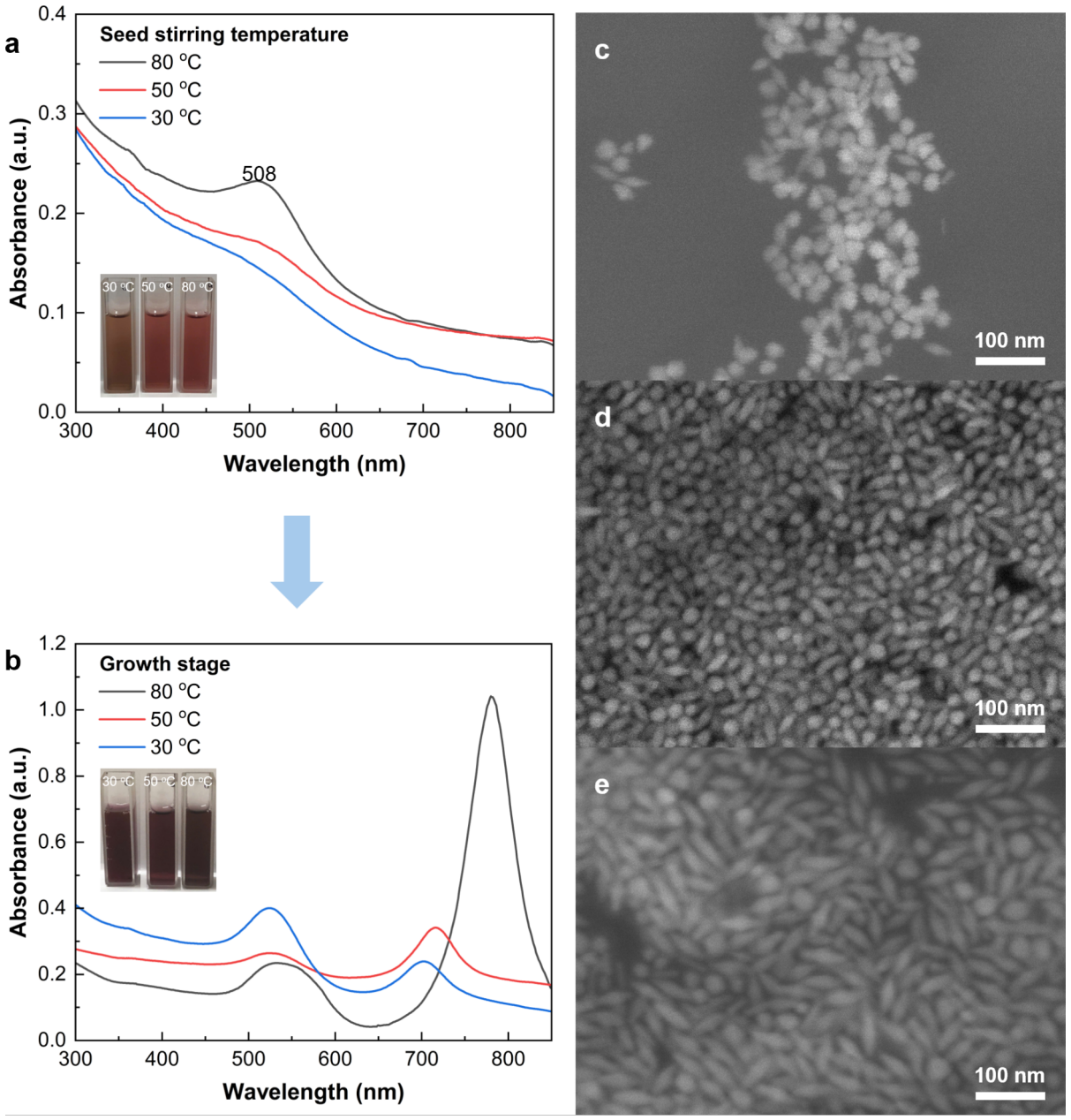


Figure 1: The annealing temperature affects the efficiency of AuBP formation. UV–vis spectra of (a) gold seed solution aged for 120 min at different temperatures and (b) growth solution, respectively. SEM images of gold nanoparticles using 100 µL seed solution at (c) 30 °C, (d) 50 °C, and (e) 80 °C.

images (Figure 1c–e). SEM images show that the synthesis efficiency of the AuBPs increased from 15% to 76% (Supporting Information File 1, Table S1). This further confirms that the use of seed particles with a twinning plane is crucial for the formation of AuBPs.

To further evaluate the impact of the annealing process, AuBPs were synthesized from nanoseeds annealed at 80 °C for different durations (0–120 min at 15 min intervals for the seed solutions, Figure 2a; and 0, 30, 60, 90, 105, and 120 min for the AuBP colloids, Figure 2b). The UV–vis spectra of the synthesized gold nanoparticles are shown in Figure 2. The SPR absorption peak at ≈508 nm gradually became more pronounced after about 30 min of annealing. The absorption intensity gradually increased at this wavelength, reaching a constant level after 120 min. As shown in the UV–vis spectra of the

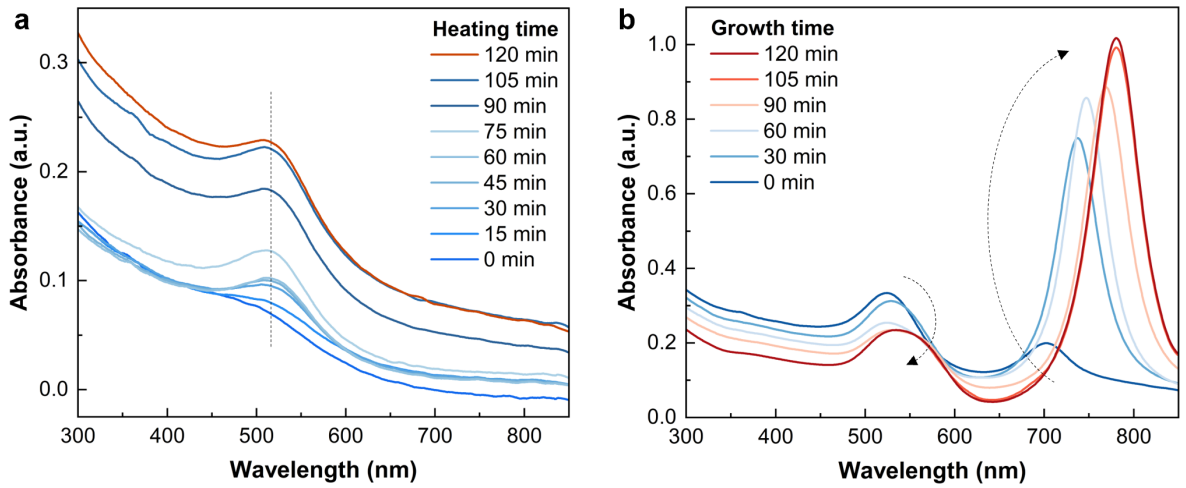


Figure 2: Effect of annealing time on AuBP formation efficiency. UV–vis spectra of (a) gold seed solution aged for different time intervals and (b) AuBP colloids synthesized with 100 µL of the corresponding seed solutions.

AuBP colloids (Figure 2b), longer annealing times resulted in the SPR absorption peaks shifting towards higher wavelengths, with stronger absorption intensity at the l-SPR peak but weaker at the t-SPR peak. This change indicates the formation of larger AuBPs with increased yield. Thus, the annealing process induced structural and morphological changes in the seed crystals. For short annealing times, the ratio [l-SPR]/[t-SPR] was ≈2.9 (gold seed crystal annealing conditions of 30 min), while for long annealing times of 60 min or more, the ratio [l-SPR]/[t-SPR] increased steadily to 5.0–5.2 after 120 min. The ratio obtained from this UV–vis spectrum is comparable to those of high-quality AuBPs reported in previous publications [22,37,38]. According to the study by Sánchez-Iglesias et al. [25], the annealing process showed a competition between size growth and twinning defect formation on the gold seed crystals. During the initial incubation period, the thermal energy primarily increased the nanoseeds' size, and the twinning defect had not yet fully occurred (0 and 15 min). Once the nanoseeds reached a certain size, the twinning defect-formation process gradually became more dominant than the size-growth process. At this point, the fraction of twinned nanoseeds became stable at 120 min. Once the growth process was complete and stable, the bipyramidal nanoparticles would have a defined and more uniform shape. However, the development of the twinning seeds simultaneously increased the size of the by-products, resulting in large, polyhedral seeds and a flattened, less sharp t-SPR peak.

Effects of surfactant used in the nanoseed synthesis: The formation of twin defects during heat treatment requires the presence of citric acid (5 mM) and CTAC (50 mM). CTAC is a cationic surfactant capable of creating stable micelles in solution and adsorbing onto the surface of newly formed gold particles via quaternary ammonium groups. Citrate ions, which contain carboxyl groups, can form weak complexes with gold ions, helping stabilize the reduction rate of the strong reducing agent $NaBH_4$ [39-41]. Furthermore, citrate ions are also a major factor in the formation and maintenance of twin defects. Citrate ions can adsorb on different planes of Au(100), Au(110), and Au(111). The adsorption of citrate ions is highly concentrated on the Au(100) and Au(110) facets, inhibiting the deposition of Au atoms during particle formation. At this point, clusters tend to develop along the ⟨111⟩ direction, forming larger seeds. The distribution of the CTAC surfactant with the citrate ion on the surface of the weakly adsorbing (111) facet, compared to the (100) and (110) facets, creates favorable conditions for the formation of gold seeds that are preferably encased by (111) planes [26].

Changing the halide group in the surfactant also affects the yield of the twinned seed. The results in Figure 3 compare the UV–vis spectra of AuBPs synthesized using nanoseed in CTAB and CTAC, while keeping other parameters unchanged. No significant changes in the seeds were observed under the two surfactant conditions, and the SPR absorption peak was observed at 508 nm. However, the presence of bromide ions resulted in an AuBP synthesis yield of only 58.3%, with a less well-defined bipyramidal morphology (see Supporting Information File 1, Figure S1 and Table S1). This was also observed in the UV–vis spectra of the growth solution: The l-SPR peak intensity of the particles using seed-CTAC was almost double that of those using seed-CTAB, and the FWHM was narrower, indicating

that the formed AuBPs might have higher monodispersity. This can be explained by the fact that the affinity and binding energy of bromide ions to the gold surface are much stronger than those of chloride ions. When CTAB is used at this stage, Br^- ions with a strong binding affinity completely cover and encapsulate the seed surface; this physical interference could reduce the formation of twinning structures, thereby reducing the formation of AuBPs.

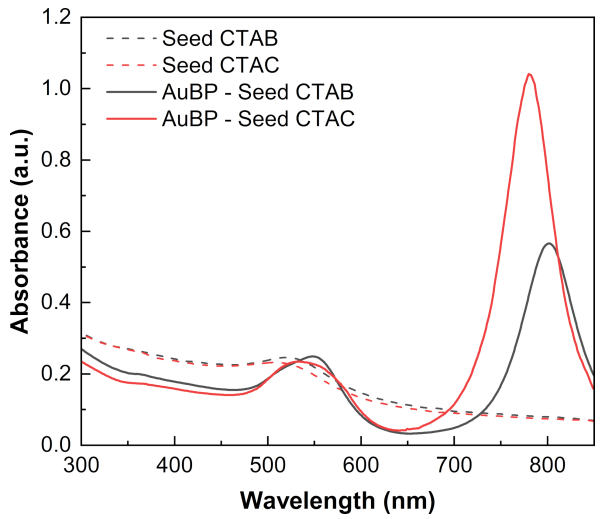


Figure 3: UV–vis spectra of aged seed solutions using different surfactants (dashed lines) and AuBP colloids synthesized with 100 µL of the corresponding nanoseed colloids (solid lines).

Effects of growth conditions

Effects of surfactant concentration: During the growth stage, surfactants play an irreplaceable role in directing anisotropic structures such as rods or bipyramids. The presence of these compounds helps stabilize the colloid because the positively charged surfactant layer adsorbed on the particle surfaces creates electrostatic repulsion between particles, preventing them from colliding and agglomerating, thus ensuring stable dispersion of the system. Furthermore, the CTAB surfactant participates in controlling the selective adsorption on different crystal planes of the particles, disrupting symmetry and orienting the structure.

The effect of changes in the concentration of CTAB in the growth solution are shown in Figure 4a and Supporting Information File 1, Figure S2. The results indicate significant variations in the position and shape of the SPR peaks as the CTAB concentration changes during particle growth. At low CTAB concentration (50 mM), the l-SPR band shows the highest intensity at 800 nm, indicating the development of anisotropic morphology. However, SEM images (Supporting Information File 1, Figure S2a) reveal that the obtained product forms not only bipyramidal but also elongated shapes, such as rice grain-like particles, along with polyhedral particles. At low CTAB concentrations, the number of CTAB molecules adsorbed onto the nanoparticle surfaces is insufficient. The uneven distribution of CTAB across crystal planes and among nanoparticles results in the simultaneous growth of the (110) and (100) planes, along with the (111) plane. Low surfactant concentrations lead to nanoparticle aggregation via van der Waals forces

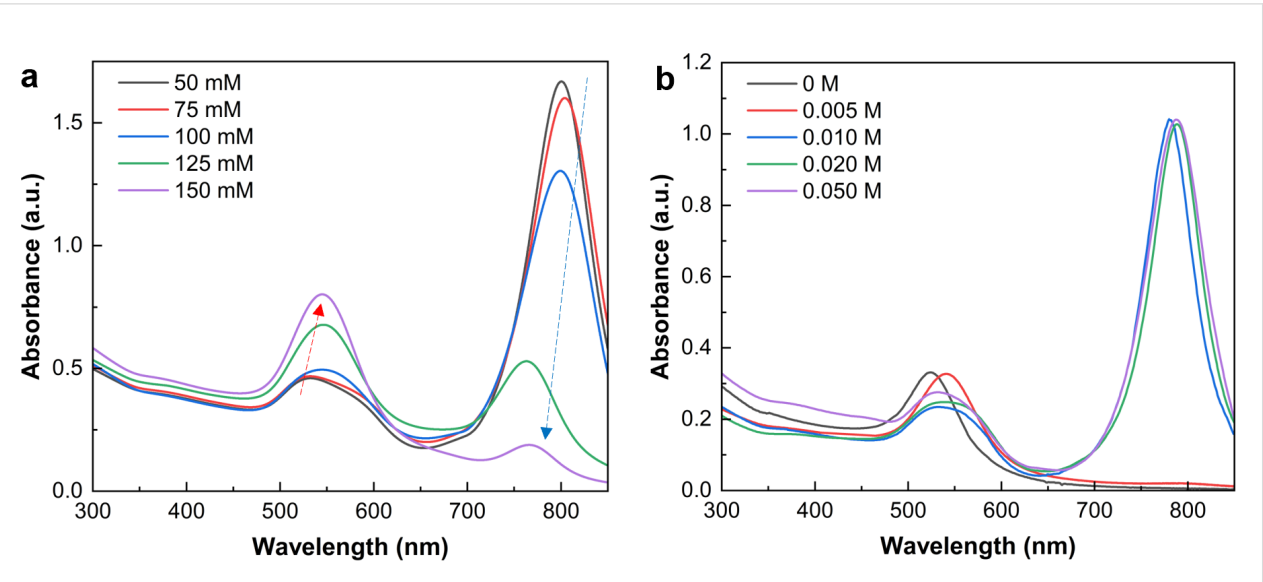


Figure 4: UV–vis spectra of AuBP colloids synthesized (a) with different concentrations of CTAB surfactant from 50 mM to 150 mM; (b) with varying $AgNO_3$ concentrations from 0 to 0.050 M.

[42]. As a result, the growth phase tends to produce by-products such as rice grain-like shapes with elongated (100) faces or polyhedral shapes with rough surfaces. Conversely, at the appropriate CTAB concentration (100 mM), selective adsorption on the lateral faces is enhanced, helping to maintain a higher vertical growth rate of the penta-twinned seed and promoting the formation of highly uniform AuBPs. However, when CTAB concentrations are too high, the micelle layer covering the surface becomes thicker, reducing the diffusion rate of Au(I) complexes to the growth surface. This can slow growth or cause dynamic imbalances among different crystal planes. UV–vis spectral observations show a significant wavelength shift, with the t-SPR peak exhibiting high absorption intensity, while the l-SPR peak is no longer clearly visible. Furthermore, excessive bromide adsorption can reduce the growth rate at the pointed ends of AuBPs, leading to blunted, non-pointed particle tips (Supporting Information File 1, Figure S2b).

Effects of $AgNO_3$ concentration: Ag^+ ions play an important role in the directional growth of AuBPs. To investigate the influence of Ag^+ ions on the formation of AuBPs, experiments were conducted with the same volume of $AgNO_3$ at different concentrations of 0, 0.005, 0.010, 0.020, and 0.050 M. The morphological and optical property changes of the material are shown in the UV–vis spectra and SEM images in Figure 4b and Supporting Information File 1, Figure S3. In the absence of $AgNO_3$, the UV–vis spectrum only showed one peak at a wavelength of 524 nm. Pseudospherical polyhedra formed when Ag^+ ions, which usually serve as inhibitors and restrict horizontal growth, were absent (Figure 4b, Supporting Information File 1, Figure S3a). This can be explained by the deposition process occurring more quickly for the newly generated Au^0 atoms on the seed surface in the absence of Ag^+, leading to uniform, isotropic formation. As the $AgNO_3$ concentration in the studied samples is gradually increased from 0.010 M, the UV–vis spectrum shows the appearance of two characteristic peaks with only slight shifts (Figure 4b). SEM images show that increasing the $AgNO_3$ concentration increases anisotropic growth. As a result, particles have a more characteristic and sharper bipyramidal morphology (Supporting Information File 1, Figure S3b).

Effects of seed volume: The size of AuBPs is significantly influenced by the volume of seed solution added during growth. This is directly related to the ratio of gold precursor to seed present in the reaction system $[Au^{3+}]/[Au^0]$. As the number of nanoseeds in the solution increases, the amount of Au^0 atoms deposited per particle decreases, leading to the formation of smaller AuBPs. Conversely, as the seed volume decreases, there are fewer growth centers, allowing more Au^0 atoms to be deposited per particle and leading to larger AuBPs.

To investigate the effect of seed volume on AuBP formation, different growth solutions were prepared with seed volumes of 100, 150, 250, 500, and 750 µL. The UV–vis spectra and SEM images are shown in Figure 5 and Figure 6, respectively. SEM images show that varying the volume of the seed solution allows for the control of AuBP size while maintaining its bipyramidal shape. The average length/width of AuBPs increased from (33.9 ± 2.6)/(14.3 ± 1.4) to (60.7 ± 2.4)/(21.6 ± 1.0) when the seed volume decreased from 750 to 100 µL. This increase in particle size led to a gradual increase in the aspect ratio of the particles from 2.4 to 2.8, as illustrated in Figure 6f and Supporting Information File 1, Figure S4. In addition, varying the volume of the seed solution not only changed the particle size in length and/or width but also affected the morphology of the tip of the AuBPs. Specifically, at the largest seed volume (750 µL), the AuBP particles obtained were truncated at both tips and had a less sharp particle morphology. Conversely, with a lower seed volume, particularly at 100 µL, the AuBP particles showed distinctly sharp, pointed ends and the characteristic bipyramidal shape.

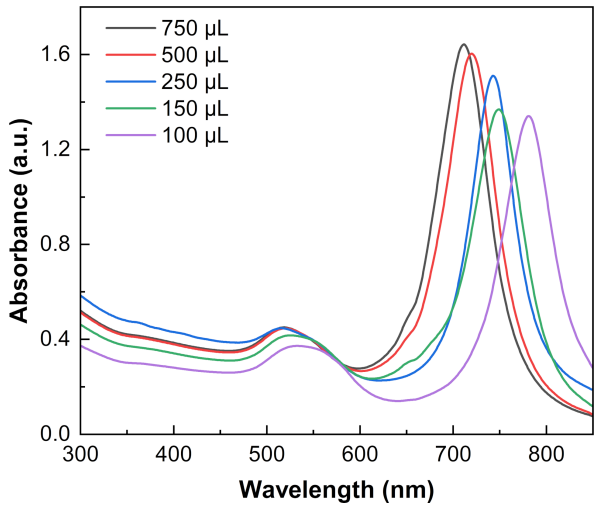


Figure 5: UV–vis spectra of AuBP colloids synthesized with different seed volumes.

Changes in the morphology and size of AuBPs are clearly reflected in the absorption spectrum. In the experimental studies, the $[Au^{3+}]/[Au^0]$ ratio increased, and the l-SPR shifted significantly to longer wavelengths from 711 to 780 nm, while the t-SPR increased only slightly from 518 to 527 nm. This result is consistent with the increased particle size observed in the FESEM images mentioned above. In addition, a shoulder was observed at the t-SPR peak, which corresponds to the SPR peak of by-products in the synthesis process [37,43]. Within appro-

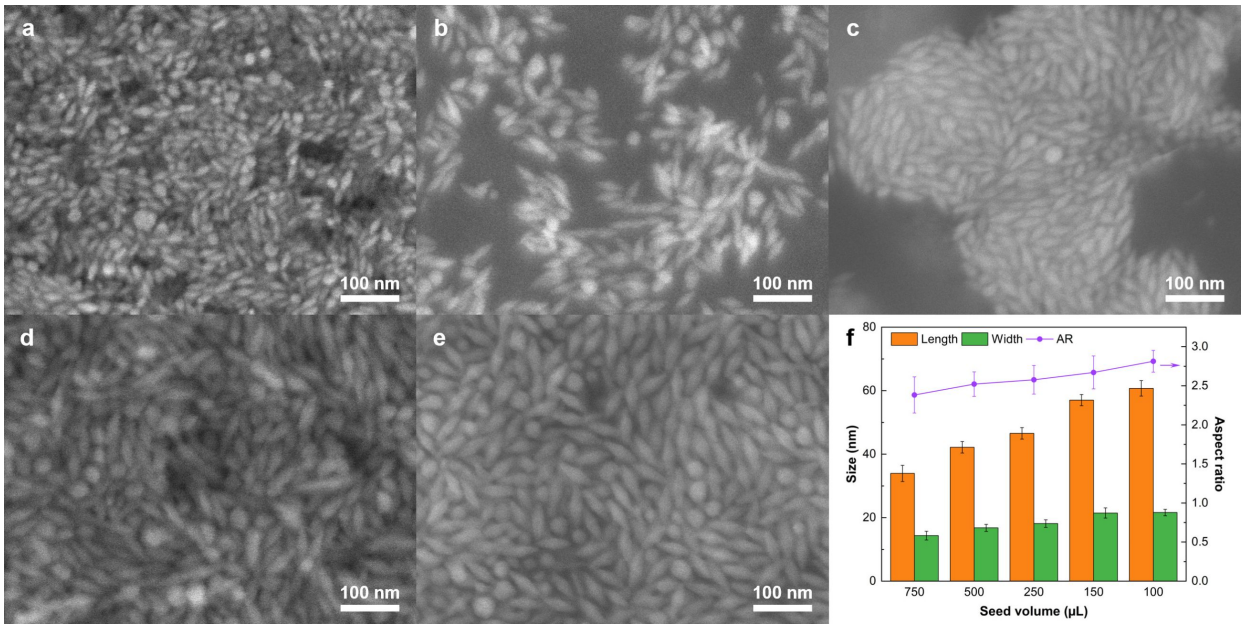


Figure 6: SEM images of AuBPs synthesized with different seed volumes: (a) 750, (b) 500, (c) 250, (d) 150, and (e) 100 µL. (f) AuBP particle size distributions and aspect ratios determined from SEM image results.

priate seed volume ranges, the formation of AuBPs with more uniform shape and size is possible, thereby increasing the material's monodispersity [24]. Within the surveyed range, all AuBPs obtained had relatively high formation efficiencies of 67–76% (Supporting Information File 1, Table S2). This indicates that the synthesis process is stable and suitable for further SERS studies and applications.

Structural and compositional characterization

The crystal structure of AuBPs was determined by XRD. The results are shown in Supporting Information File 1, Figure S5. The diagram shows high-intensity diffraction peaks at 2θ values of 38.1°, 44.4°, 64.6°, and 77.5° corresponding to the lattice planes (111), (200), (220), and (311) of the face-centered cubic (FCC) crystal structure of gold in accordance with the JCPDS database (no. 65-8601) [22,44]. The diffraction peak at 2θ = 38.1° has the highest intensity, indicating that the gold nanobipyramid structure is preferentially oriented to grow along the (111) plane, consistent with the anisotropic growth mechanism of AuBPs discussed in Section "Formation mechanism".

The crystal structure of AuBPs was further analyzed by HRTEM and SAED, as shown in Figure 7. The magnified image clearly shows lattice patterns at the particle's tip and body. These lattice patterns are parallel to the particle's growth axis and have a twinned structure along the long axis. In both the tip (Figure 7b) and middle (Figure 7c) regions, lattice spacings (d) of, respectively, 0.242 and 0.211 nm were determined, corresponding to the (111) and (200) crystal planes of the bipyramidal particle [22]. The SAED analysis in Figure 7d shows the reflection points numbered according to the lattice plane distances: $d_{(111)}$ = 2.36 Å, $d_{(200)}$ = 2.04 Å, $d_{(220)}$ = 1.43 Å, $d_{(311)}$ = 1.23 Å, $d_{(400)}$ = 1.02 Å, and $d_{(420)}$ = 0.91 Å. All measured values have a deviation of no more than ±3% from the bulk crystal data of gold and are consistent with previously published results [45,46]. This indicates that the AuBPs, after synthesis, have a penta-twinned structure with a FCC lattice. It should be noted that Ag could not be distinguished in the HRTEM images and SAED pattern. Both Ag and Au crystallize in the FCC structure with nearly identical lattice constants (4.086 Å for Ag and 4.079 Å for Au), so the lattice fringes and diffraction spots of trace Ag deposited on the AuBPs' surface overlap with those of Au. Therefore, the presence of Ag was further examined by EDS mapping and XPS analysis, as discussed below.

The elemental composition of the AuBPs was analyzed using EDS. As shown in Figure 8a, the EDS spectrum recorded a characteristic Au signal, including an M-shell signal in the low-energy region (≈2.1 keV) and L-shell signals in the higher-energy region (≈8.5–12.5 keV). The clear and prominent presence of these peaks confirms that the main component of the sample is gold [47,48]. Since the EDS analysis was mainly used to determine the elemental composition, the SEM image for

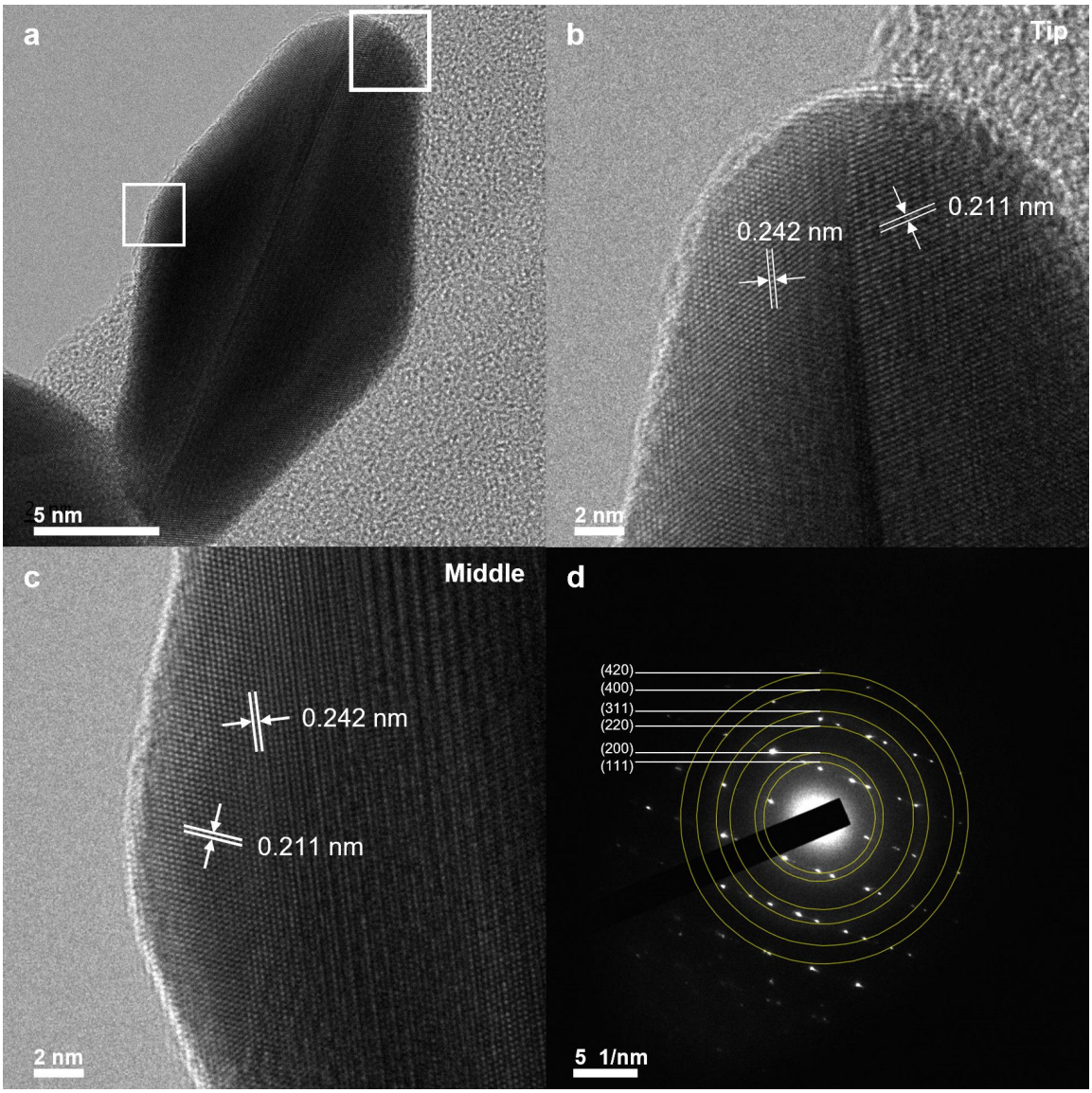


Figure 7: (a) HRTEM image of a AuBP; magnified images showing the lattice fringes of the areas marked with white boxes at (b) the tip and (c) the middle of the AuBP. (d) SAED pattern of the AuBP.

elemental mapping was recorded at a lower magnification over a densely packed AuBP region to obtain sufficient elemental signals (Figure 8b). Therefore, the bipyramidal morphology of individual particles is less distinguishable than in the high-magnification SEM images in Figure 6. The elemental distribution map of gold in Figure 8g shows that the Au-M signal (purple) is uniformly and clearly distributed in the geometric region of the AuBP particles, while the surrounding background shows no significant gold signal. This result indicates that gold is selectively distributed within the particle structure region, without spreading into the surrounding background, and reflects a high degree of chemical homogeneity in the material.

In addition to Au, the results also show peaks for Ag, Br, O, and C. The appearance of Ag can be explained by its role in directing the anisotropic growth of the gold nanoparticles. The Ag distribution map (Figure 8f) shows that Ag is concentrated in the same region as Au atoms, demonstrating that Ag is directly associated with the bipyramidal gold nanoparticle structure, consistent with the growth mechanism discussed in Section “Formation mechanism”. The elements Br and C originate from the CTAB surfactant used in the synthesis. Additionally, the oxygen signal may originate from oxygen species adsorbed during the sample’s exposure to air. The distribution maps of C, O, and Br are shown in Figure 8c–e.

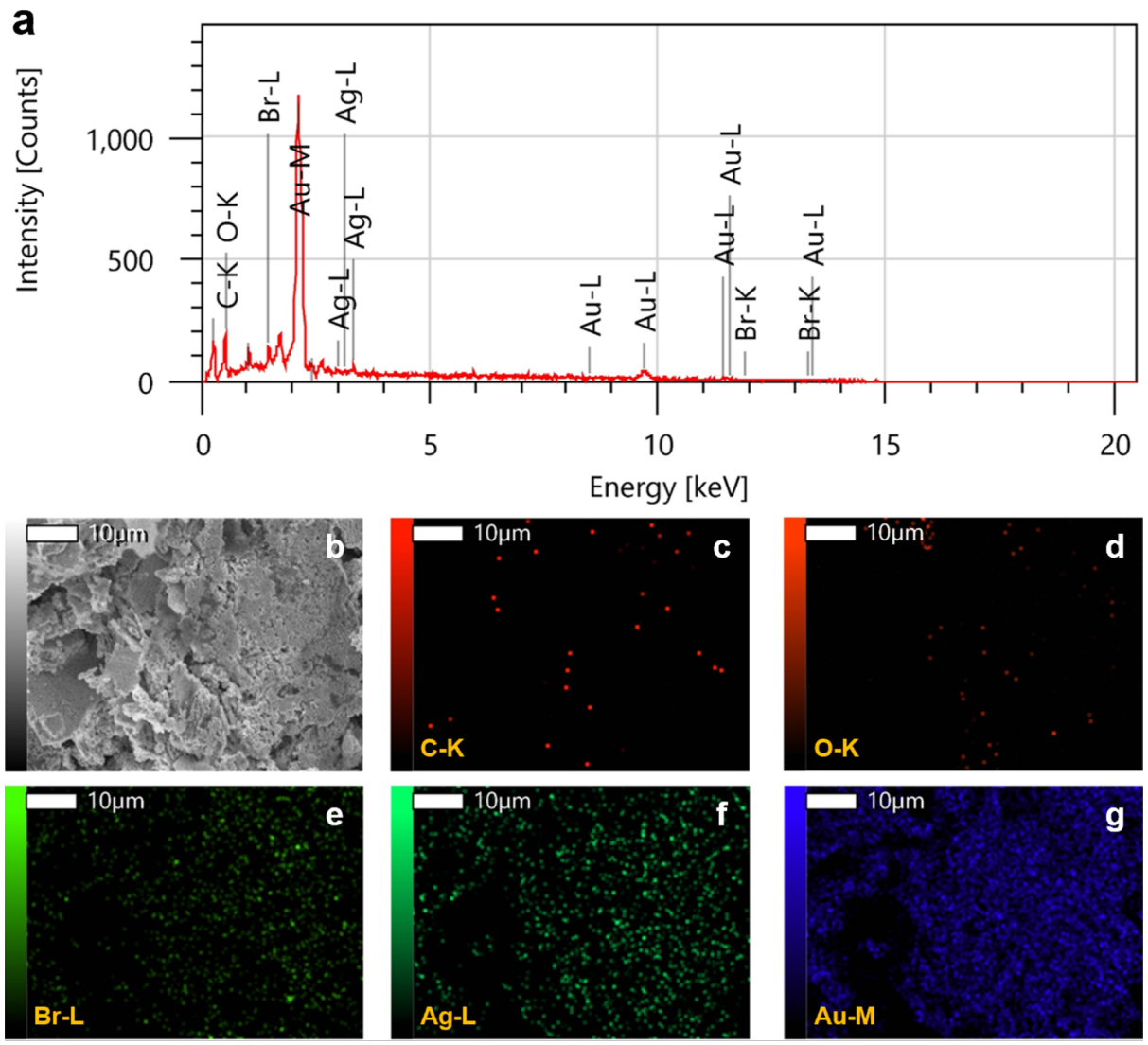


Figure 8: (a) EDS spectrum and (b) low-magnification SEM image and elemental mapping (c) C, (d) O, (e) Br, (f) Ag, and (g) Au of AuBPs.

XPS was used to determine the elemental composition and surface chemical state of the bipyramidal gold nanomaterial (Figure 9). The survey spectrum in Figure 9a shows characteristic signals of the elements Au, Ag, O, C, and Br. The Au 4f and Ag 3d signals confirm the presence of gold and silver on the material surface, while the C 1s and Br 3d signals are related to the residual CTAB surfactant layer on the particle surface after synthesis. The high-resolution XPS spectrum of Au 4f (Figure 9b) shows two characteristic peaks at 87.4 and 83.7 eV, corresponding to the Au $4f_{5/2}$ and Au $4f_{7/2}$ energy levels, respectively, with a spin–orbit splitting of ≈3.7 eV. This result indicates that the Au component in the AuBPs structure exists primarily in the Au^0 state [49]. Furthermore, no other significant signal components were observed in the higher-binding-energy regions corresponding to the Au^+ or Au^{3+} oxidation states. Thus, the Au precursor was completely reduced during synthesis. For the Ag 3d spectrum, signals were recorded at approximately 373.6 and 367.6 eV for Ag $3d_{3/2}$ and Ag $3d_{5/2}$, respectively, with an energy separation of ≈6.0 eV, characteristic of metallic silver [50,51]. The presence of Ag atoms on the AuBPs' surface is consistent with the growth mechanism proposed in Section "Formation mechanism".

In the HRXPS spectrum, C 1s peaks appear at 284.8 and 286.4 eV, assigned to C–C and C–$N^+(CH_3)_3$ bonds, respectively. In addition, peaks at 67.9 and 69.0 eV of Br 3d appear due to the presence of surfactants on the nanoparticle surface [51]. The O 1s spectrum (Figure 9d) shows a peak at 531.4 eV assigned to C–O bonds of residual organic species [52], a peak at 532.7 eV attributed to oxygen vacancies (V_O) [53], and a peak at

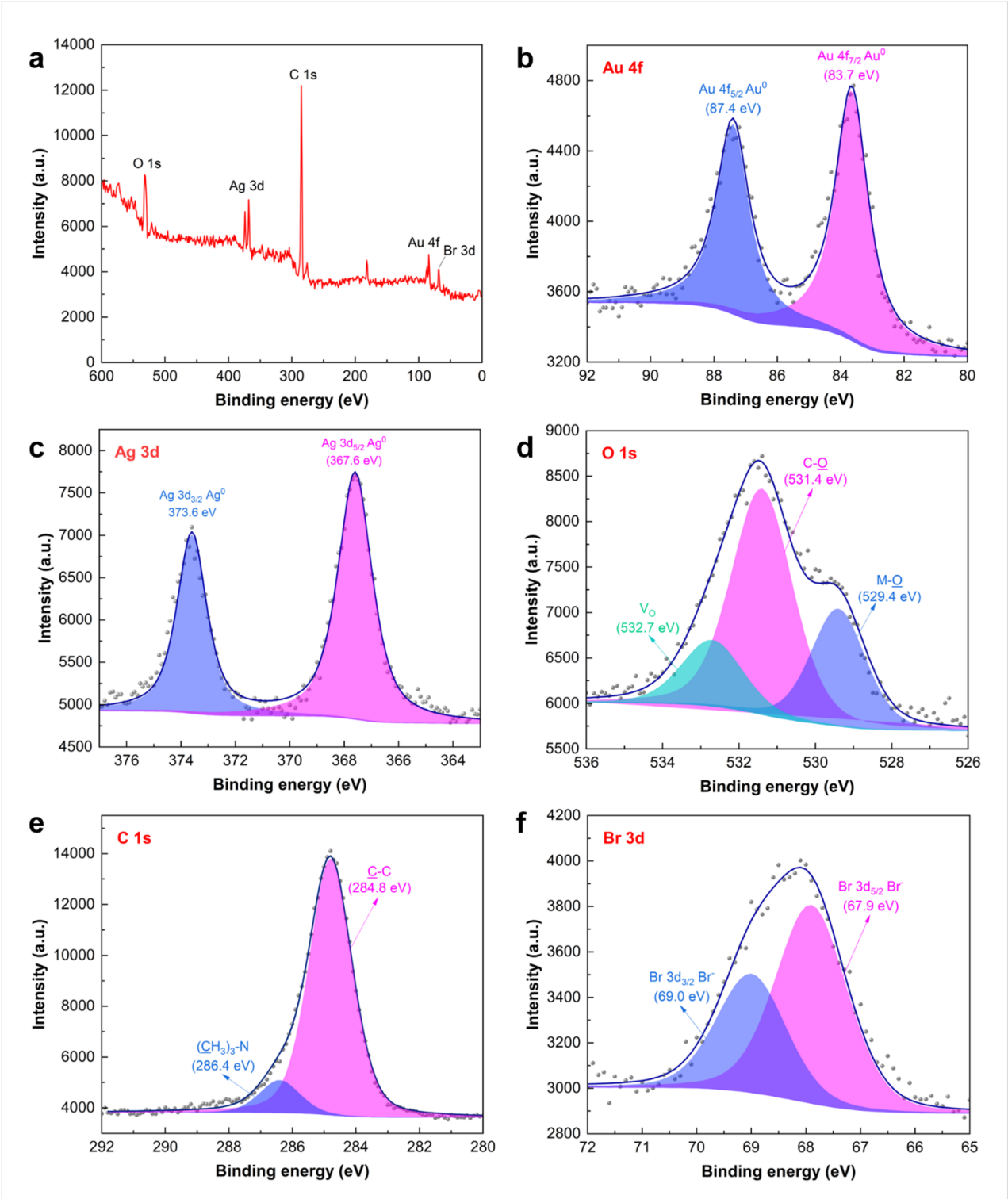


Figure 9: (a) XPS survey spectra of AuBPs and HRXPS spectra of (b) Au 4f, (c) Ag 3d, (d) O 1s, (e) C 1s, and (f) Br 3d.

529.4 eV characteristic of metal–oxygen (M–O) bonding, further validating the Ag deposition mechanism on the gold particle surface and suggesting that a small amount of silver material may have been oxidized [53].

Formation mechanism

The AuBPs were synthesized via a seed-mediated method with penta-twinned gold seed formation and anisotropic growth. In this process, the penta-twinned nanoseeds serve as the crystalli-

zation center, directly influencing the growth efficiency and shape of the gold nanobipyramids. Nanoseeds are prepared by rapidly reducing $HAuCl_4$ with $NaBH_4$ in a solution containing the surfactant CTAC and citric acid, and heating during annealing to form the penta-twinned structure [25]. Subsequently, seeds are stabilized and further used for the growth stage. In the growth stage, the solution consists of the precursor $HAuCl_4$, the surfactant CTAB, the shape-directing agent $AgNO_3$, HCl, and the weak reducing agent AA. When using a weak reductant such as AA, Au^{3+} ions in CTAB solution at low pH form a bromide complex that can only be reduced to Au^+ (Equation 1). After adding seeds to the growth solution, the slow reduction of Au^+ to Au^0 occurs directly on the seed surface (Equation 2). This slow reduction process helps control nanoparticle growth, ensuring that gold atoms mainly deposit on seed particle surfaces rather than forming new nucleation sites in the solution. The general equation for the reduction process is given by Equation 3. The molar ratio of [AA]/[$HAuCl_4$] is 1.6 in the synthesis process to ensure complete reduction of Au^{3+} to Au^0. If the AA concentration is insufficient, unreduced Au^{3+} ions act as an oxidizing agent, leading to a competitive corrosion reaction and truncated-bipyramidal morphologies [38].

$$\begin{aligned}&\text{CTA-AuBr}_4 + \text{C}_6\text{H}_8\text{O}_6 \rightarrow \\ &\text{CTA-AuBr}_2 + \text{C}_6\text{H}_6\text{O}_6 + 2\text{H}^+ + 2\text{Br}^-\end{aligned} \quad (1)$$

$$\begin{aligned}&2\text{CTA-AuBr}_2 + \text{C}_6\text{H}_8\text{O}_6 \rightarrow \\ &2\text{Au}^0 + \text{C}_6\text{H}_6\text{O}_6 + 2\text{CTA}^+ + 2\text{H}^+ + 4\text{Br}^-\end{aligned} \quad (2)$$

$$\begin{aligned}&2\text{CTA-AuBr}_4 + 3\text{C}_6\text{H}_8\text{O}_6 \rightarrow \\ &2\text{Au}^0 + 3\text{C}_6\text{H}_6\text{O}_6 + 2\text{CTA}^+ + 6\text{H}^+ + 8\text{Br}^-\end{aligned} \quad (3)$$

The selective deposition of newly formed gold atoms onto the seed surface is facilitated by the surfactant CTAB and the Ag^+ ions. CTAB is a cationic surfactant that stabilizes nanoparticles by forming a positively charged layer around them, thereby preventing aggregation [54,55]. In addition, $[AuCl_4]^-$ ions added to the solution undergo ligand exchange with Br^- to form the $[CTA]^+[AuBr_4]^-$ bromide complex. The Br^- ions tend to selectively adsorb on the (100) facets of the gold seed, thus causing CTA^+ to form a micelle layer on this plane, leading to anisotropic growth [35,54]. In the presence of Ag^+, underpotential deposition on the surface of gold particles occurred on the (110) and (100) facets rather than the (111) facets [23,25]. This results in gold atoms preferentially depositing on the (111) crystal surface, promoting growth along the ⟨110⟩ direction and forming pentagonal bipyramids. Therefore, the final shape of AuBPs depends on synthetic parameters, including seed formation conditions, surfactant concentration, Ag^+ ion concentration, and seed solution volume. Controlling these factors allows for tuning size, shape, and plasmon properties of the nanomaterial.

FDTD study

A 3D model of the AuBPs was constructed based on the average sizes obtained from the SEM results of the samples synthesized with 750, 500, 250, 150, and 100 µL. Electric field intensity and distribution of the AuBPs were calculated using 3D FDTD simulations at excitation wavelengths corresponding to the experimental conditions, as shown in Figure 10. Under ideal conditions, when the excitation light direction was set perpendicular to the length axis, with the electric field aligned along the length axis, the change of the longitudinal plasmon, which plays the dominant role in enhancing the electromagnetic signal in SERS with 1D anisotropic structures, was investigated (see Supporting Information File 1, Figure S6 for the simulation setup). Simulations showed a strong local electric-field enhancement at the particle tips, which increased with particle size across the three wavelengths investigated. The electric field enhancement capability yielded a maximum value of $|E/E_0|_{max}$ = 34.43 (for the 100 µL nanoseed volume) at an excitation wavelength of 638 nm [56]. There is a significant change in the electric field distribution when the simulation medium is changed to n = 1.33, corresponding to water conditions (Supporting Information File 1, Figure S7). In water, the strongest local electric fields were obtained for the smallest AuBPs (750 µL nanoseed volume) at 638 nm ($|E/E_0|_{max}$ = 36.91) and for the largest AuBPs (100 µL nanoseed volume) at 785 nm ($|E/E_0|_{max}$ = 30.54). This phenomenon could be explained by an increase in the refractive index, which redshifts the l-SPR of AuBPs, so that the l-SPR of each AuBP size matches a different excitation wavelength. In addition, at all three wavelengths surveyed (532, 638, and 785 nm), the electric fields consistently concentrate at the two pointed ends of the AuBPs, indicating the dominance of the lightning-rod effect. The simulation findings closely match the experimental results and were used to select the optimal conditions for preparing the AuBP substrate for subsequent SERS applications.

SERS detection of malachite green

Due to their plasmonic properties and unique morphology, AuBPs are promising SERS substrates. A 10^{-5} M MG solution was subjected to SERS analysis on the AuBP substrate using 532, 638, and 785 nm Raman lasers to select the appropriate wavelength for detection (Supporting Information File 1, Figure S8). Raman spectra show that the 638 nm laser provides the greatest signal enhancement under the experimental conditions. The 638 nm laser effectively excites the LSPR oscillation of the AuBP substrate, which also resonates well with the electronic

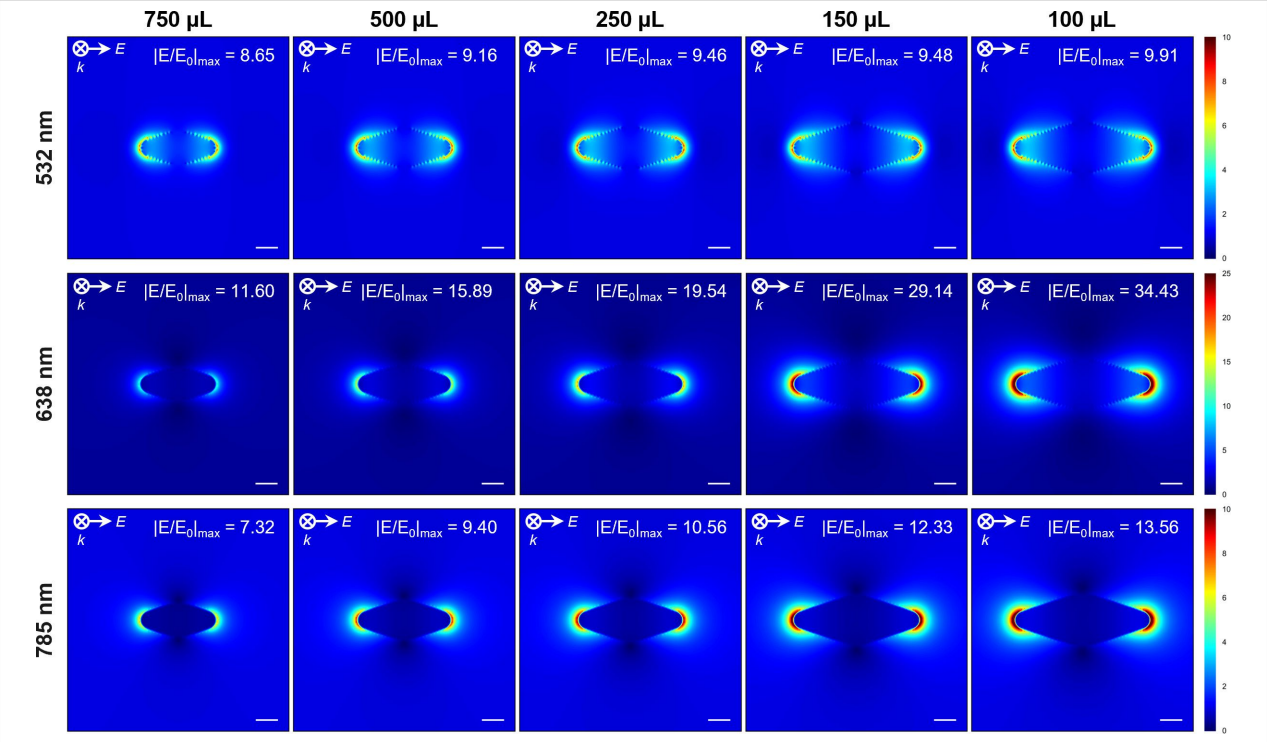


Figure 10: Electric field distribution of the AuBPs at experimental Raman excitation wavelengths with the 3D model built from SEM images. The refractive index of the medium was set to 1 to mimic air, the dispersion medium for the AuBPs in the SERS experiment.

state of the malachite green molecule [57]. At 532 nm, the analyte signal is absent, possibly due to the interband transition of gold, which converts the optical field into thermal energy rather than enhancing the local electric field on the AuBP substrate [58]. Conversely, at a laser wavelength of 785 nm, Raman scattering decreases according to the law $I \sim 1/\lambda^4$ [59], so the signal intensity obtained at 785 nm is lower than that obtained at 638 nm. Therefore, the 638 nm laser was used for all subsequent SERS measurements of MG.

A comparative investigation of the Raman spectra of the AuBP substrate, 10^{-2} M MG on a glass slide (normal Raman), and 10^{-5} M MG on the AuBP substrate is shown in Supporting Information File 1, Figure S9. The details of peak frequencies and vibration assignment in the Raman signal of the malachite green molecules are provided in Supporting Information File 1, Table S3. The spectra of the 10^{-5} M MG sample on the AuBP substrate exhibit characteristic vibrational bands with high intensity. Meanwhile, the spectra of the 10^{-2} M MG sample also display signals at the same Raman shift but with significantly lower intensity. This demonstrates that the AuBP substrate plays a crucial role in enhancing SERS by providing distinct LSPR. Furthermore, the Raman spectrum of the AuBP substrate did not exhibit characteristic peaks in the investigated region, indicating that the material itself did not generate significant Raman signals and did not interfere with analyte detection.

The intensity of the Raman signals at 1170 and 1617 cm^{-1}, corresponding to, respectively, in-plane aromatic C–H vibration of the ring ($\delta_{in}(C–H)_{ring}$) and ring C=C stretching ($\nu(C=C)_{ring}$), were used to estimate the enhancement factor (EF) value [60,61]. The EF value for the AuBPs was calculated to be 2.5×10^6 (for 1170 cm^{-1}) and 3.9×10^6 (for 1617 cm^{-1}) (Supporting Information File 1, Equation S1, section "Enhancement factor determination"). The detection capability of the AuBP substrate for MG was investigated over a concentration range of 10^{-9} M to 10^{-5} M. SERS spectra and the characteristic peak of AuBP-MG are shown in Figure 11. The Raman intensity of MG signals on the SERS substrate decreases with a decrease in MG concentration. The Raman signal of MG was still observed at a trace concentration of 10^{-9} M. The signal intensity changes regularly with the logarithm of MG concentration; therefore, above MG concentration range was used to construct the SERS calibration curve. The linear relationship of intensity with log C was determined at two characteristic MG signal positions at 1170 and 1617 cm^{-1}, as shown in Supporting Information File 1, Figure S10. In particular, within the investigated MG concentration range, two calibration curves are observed at two independent Raman peaks, demonstrating the high reliability of the analytical method when using the AuBP substrate (Supporting Information File 1, Figure S10). A weak Raman feature was observed at $10^{-9.5}$ M; however, its signal-to-noise ratio (S/N) was less than 3, so the signal could not be confidently distin-

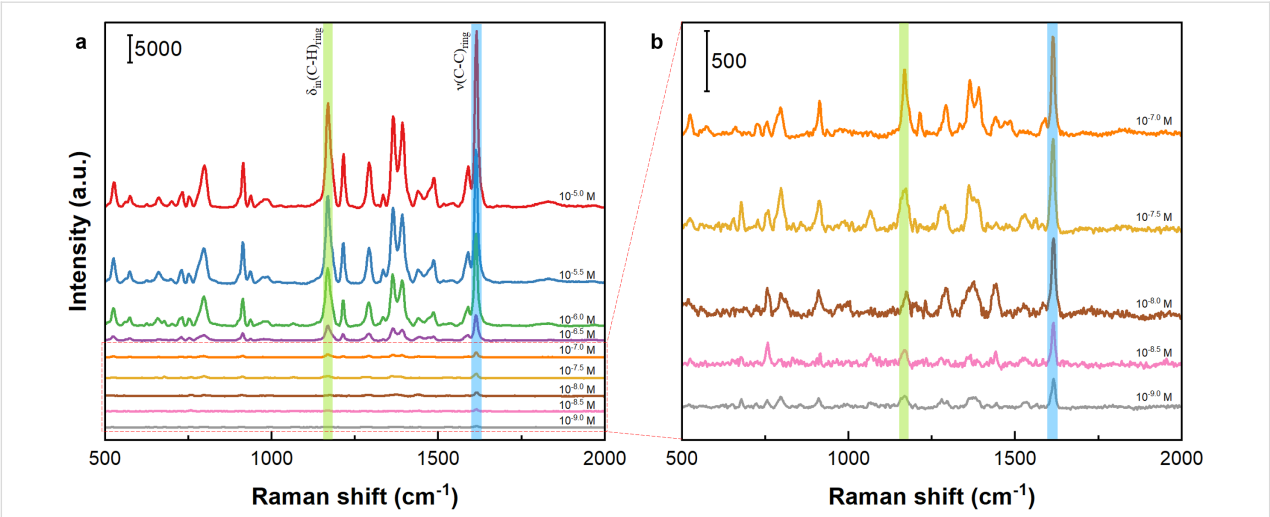


Figure 11: Raman spectra of MG on AuBP substrates (a) from $10^{-9.0}$ M to $10^{-5.0}$ M and (b) from $10^{-9.0}$ M to $10^{-7.0}$ M.

guished from background noise (Supporting Information File 1, Figure S11). Therefore, the limit of detection (LOD) was determined as 10^{-9} M, corresponding to the lowest concentration that produced a Raman signal with $S/N \geq 3$ (Supporting Information File 1, Figure S11). The SERS enhancement effect of the AuBP substrate is due to its bipyramidal structure with two tips. A nanogap forms between the AuBPs at the tips, creating strong, high-intensity "hot spots" that significantly increase the Raman scattering intensity of adsorbed molecules [19,62]. In addition to the electromagnetic mechanism, the adsorption of MG molecules onto the gold surface also contributes to the SERS signal. MG exists as a cationic dye in aqueous solution and can therefore be readily attracted to the AuBPs' surface, where bromide ions remain adsorbed after the removal of excess CTAB (Figure 9f). According to Qian et al., the electronic structure of MG adsorbed on gold nanoparticles remains sensitive to pH and can be switched between its localized and delocalized forms, unlike that of its isothiocyanate derivative (MGITC), which is irreversibly "locked" on the gold surface. This suggests that MG interacts with the gold surface through relatively weak electronic coupling [63]. In addition, density functional theory calculations of MG adsorbed on Fe_3O_4@Au composite nanospheres yielded a SERS spectrum very close to the experimental one, supporting the enhancement of MG adsorbed on the gold surface [64]. Thus, the adsorption of MG molecules near the hot spots at the AuBPs tips, combined with the strong electromagnetic enhancement, contributes to the characteristic SERS signal of MG.

The repeatability of the Raman signal of MG on the AuBP substrate was investigated at 20 random points on two substrates under the same preparation conditions. An MG solution at 10^{-7} M was used for the investigation because this concentration lies at the transition point between the two linear ranges (10^{-9}–10^{-7} M and 10^{-7}–10^{-5} M, Supporting Information File 1, Figure S10). At this concentration, the Raman signals are strong enough to evaluate signal variations while the influence of background noise is minimized. The results are shown in Figure 12. Raman signals of MG are observed, especially at 1170 and 1617 cm^{-1}, with signal intensities within acceptable limits. Figure 12b,c shows relatively low relative standard deviation (RSD) values of 13.45% at 1170 cm^{-1} and 8.34% at 1617 cm^{-1} (Supporting Information File 1, Tables S4 and S5), indicating that the SERS intensity was relatively consistent among the measured points. The sample measurement on two SERS substrates shows repeatability after each laser exposure, demonstrating the substrate's high durability.

To evaluate the practical applicability of the AuBP substrate in detecting MG in real water samples, MG solutions were mixed with each type of $CaCl_2$, $MgSO_4$, $NaNO_3$, and $NH_4H_2PO_4$ salts at a final MG concentration of 10^{-7} M and a final salt solution concentration of 10^{-5} M. The results are shown in Supporting Information File 1, Figure S12a, indicating that at 1617 and 1170 cm^{-1}, the SERS intensity of MG on the AuBP substrate, with or without ion presence, was similar and showed no significant difference. However, when $FeCl_3$ or $AlCl_3$ was present, the signal intensity decreased markedly (by approximately 35–60%). This could be due to Fe^{3+} or Al^{3+} ions complexing with MG, affecting the SERS signal obtained. The results showed that the AuBP substrate was almost unaffected by alkali and alkaline-earth metal ions such as Na^+, Ca^{2+}, and Mg^{2+}. These ions did not degrade the SERS signal intensity of MG, demonstrating the potential of the AuBP substrate for detecting MG in aquaculture water samples in practical applications. Furthermore, the SERS substrate containing the 10^{-7} M MG

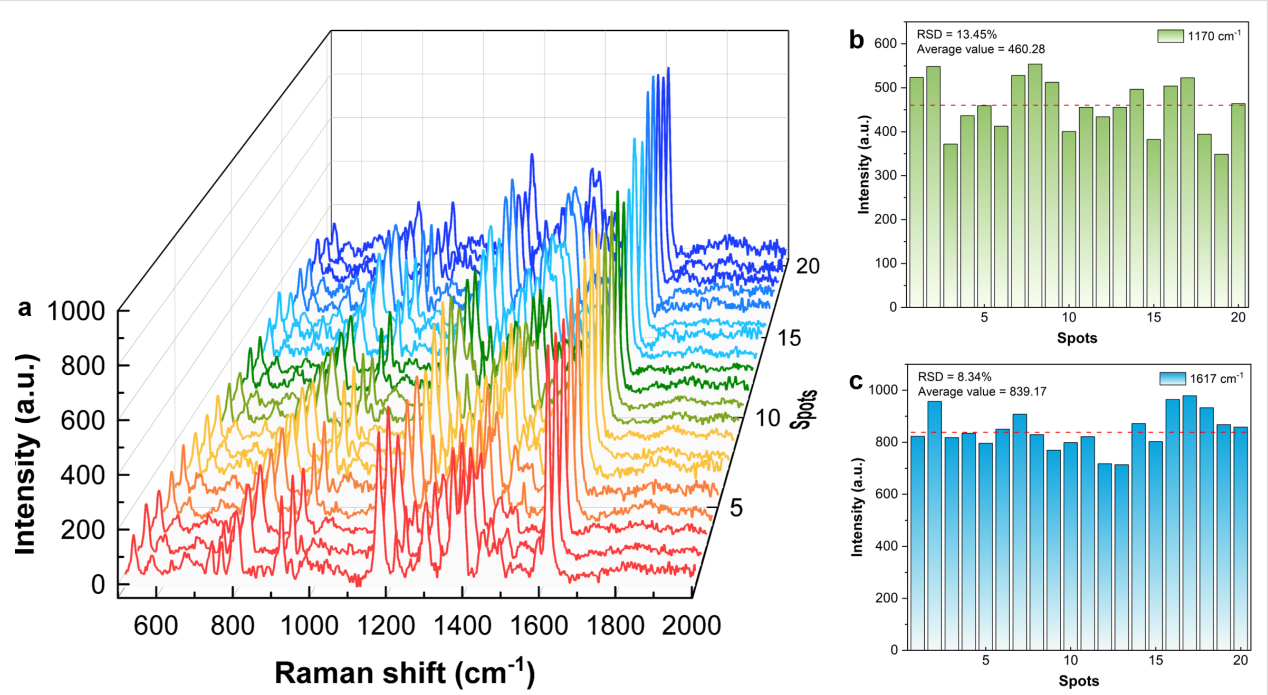


Figure 12: (a) SERS spectra of 10^{-7} M MG at 20 random points on two AuBPs SERS substrates. Raman peak intensity at (b) 1170 cm^{-1} and (c) 1617 cm^{-1}.

sample was re-measured after 7 and 14 days to check its stability. The signal intensities at the two characteristic Raman peaks (Supporting Information File 1, Figure S12b) showed no significant change. This result indicates that the AuBP substrate remained stable during storage for 14 days.

The AuBP substrate was further investigated for its versatility by detecting different analytes, including the antibiotic ciprofloxacin, the dyes methylene blue and rhodamine 6G, and the thiol-containing probe molecules 4-aminothiophenol and 4-mercaptobenzoic acid. The analyte concentration was 10^{-5} M. Supporting Information File 1, Figure S13 shows that the SERS spectra of all analytes exhibit characteristic Raman peaks with clear intensities. The results show that the AuBP substrate not only enhances the signal for the probe MG but is also effective for other analytes, expanding its potential application in the detection of pollutants using SERS.

Conclusion

In conclusion, a highly controllable seed-mediated strategy was successfully developed for the synthesis of AuBPs with a high shape purity of approximately 76% by systematically regulating penta-twinned seed formation and anisotropic crystal growth. The appropriate conditions were achieved to effectively suppress isotropic by-products and promote anisotropic growth into well-defined bipyramidal nanostructures. The synthesized AuBPs exhibited an aspect ratio of 2.8, an l-SPR at 780 nm, and highly crystalline bipyramidal structures with ultrasharp tips. As SERS substrates, the optimized AuBPs enabled highly sensitive detection of MG with an LOD of 10^{-9} M and an EF of 3.9×10^6. FDTD simulations further confirmed that the remarkable Raman enhancement originated from the intense electromagnetic fields localized at the bipyramid tips, in excellent agreement with the experimental observations. This study presents a practical method for synthesizing high-quality AuBPs, highlighting their potential for ultrasensitive SERS sensing, environmental monitoring, and nanophotonics.

Supporting Information

Summary of SPR peaks and AuBPs yields (Table S1); SEM images of AuBPs synthesized with seed-CTAB and with different CTAB and $AgNO_3$ concentrations (Figures S1–S3); experimental conditions, size distributions, and aspect ratios of AuBPs synthesized with different seed volumes (Table S2, Figure S4); XRD pattern (Figure S5); FDTD simulation setup and electric field distributions in water (Figures S6 and S7); Raman spectra of MG with different excitation lasers and on glass and AuBP substrates (Figures S8 and S9); determination of the enhancement factor (Equation S1); calibration curves and LOD of MG (Figures S10 and S11); assignment of Raman and SERS bands of MG (Table S3); repeatability data (Tables S4 and

bands of MG (Table S3); repeatability data (Tables S4 and S5); interference and stability tests (Figure S12); and SERS spectra of other analytes (Figure S13).

Supporting Information File 1

Additional experimental and characterization data.
[https://www.beilstein-journals.org/bjnano/content/supplementary/2190-4286-17-115-S1.pdf]

Acknowledgements

We would like to express our sincere gratitude to the Faculty of Physics and Physics Engineering, Ho Chi Minh City University of Science, Vietnam National University, Ho Chi Minh City, for providing the Raman spectroscopy equipment that helped us successfully complete this paper.

Funding

This research received no external funding.

Conflicts of Interest

We affirm that there are no conflicts to declare.

Author Contributions

Quang Duy Nguyen: conceptualization; data curation; formal analysis; investigation; methodology; software; validation; writing – original draft; writing – review & editing. Chau-A Thi Ho: conceptualization; data curation; formal analysis; investigation; methodology; validation; writing – original draft; writing – review & editing. Lo Nu Hoang Tien: investigation; methodology; resources; validation. Dohoon Lee: investigation; methodology; resources; validation. Thi Thanh Nguyen Ho: data curation; formal analysis; investigation; methodology. Le Vinh Phong: data curation; methodology; software. Vu Thi Hanh Thu: resources; software; visualization. Hai Son Truong-Lam: investigation; methodology; resources; validation. Khuong Quoc Vo: conceptualization; funding acquisition; methodology; project administration; resources; validation; visualization. Sy Van Vu: conceptualization; investigation; methodology; project administration; resources; software; supervision; validation; visualization; writing – original draft; writing – review & editing.

ORCID® iDs

Quang Duy Nguyen - https://orcid.org/0009-0001-7665-6028
Lo Nu Hoang Tien - https://orcid.org/0000-0003-2108-6344
Thi Thanh Nguyen Ho - https://orcid.org/0000-0001-7183-3008
Le Vinh Phong - https://orcid.org/0000-0001-8689-4575
Hai Son Truong-Lam - https://orcid.org/0000-0003-2435-6039
Khuong Quoc Vo - https://orcid.org/0000-0003-1181-0458
Sy Van Vu - https://orcid.org/0000-0001-7340-0417

Data Availability Statement

All data that supports the findings of this study is available in the published article and/or the supporting information of this article.

References

1. Langer, J.; Jimenez de Aberasturi, D.; Aizpurua, J.; Alvarez-Puebla, R. A.; Auguie, B.; Baumberg, J. J.; Bazan, G. C.; Bell, S. E. J.; Boisen, A.; Brolo, A. G.; Choo, J.; Cialla-May, D.; Deckert, V.; Fabris, L.; Faulds, K.; Garcia de Abajo, F. J.; Goodacre, R.; Graham, D.; Haes, A. J.; Haynes, C. L.; Huck, C.; Itoh, T.; Käll, M.; Kneipp, J.; Kotov, N. A.; Kuang, H.; Le Ru, E. C.; Lee, H. K.; Li, J.-F.; Ling, X. Y.; Maier, S. A.; Mayerhöfer, T.; Moskovits, M.; Murakoshi, K.; Nam, J.-M.; Nie, S.; Ozaki, Y.; Pastoriza-Santos, I.; Perez-Juste, J.; Popp, J.; Pucci, A.; Reich, S.; Ren, B.; Schatz, G. C.; Shegai, T.; Schlücker, S.; Tay, L.-L.; Thomas, K. G.; Tian, Z.-Q.; Van Duyne, R. P.; Vo-Dinh, T.; Wang, Y.; Willets, K. A.; Xu, C.; Xu, H.; Xu, Y.; Yamamoto, Y. S.; Zhao, B.; Liz-Marzan, L. M. *ACS Nano* **2020,** *14,* 28–117. doi:10.1021/acsnano.9b04224
2. Schlücker, S. *Angew. Chem., Int. Ed.* **2014,** *53,* 4756–4795. doi:10.1002/anie.201205748
3. Willets, K. A.; Van Duyne, R. P. *Annu. Rev. Phys. Chem.* **2007,** *58,* 267–297. doi:10.1146/annurev.physchem.58.032806.104607
4. Kneipp, K.; Wang, Y.; Kneipp, H.; Perelman, L. T.; Itzkan, I.; Dasari, R. R.; Feld, M. S. *Phys. Rev. Lett.* **1997,** *78,* 1667–1670. doi:10.1103/physrevlett.78.1667
5. dos Santos, G. F. S.; Paganoto, G. T.; Cosme, L. C.; Prado, A. R.; Cassini, S. T. A.; Guimarães, M. C. C.; de Oliveira, J. P. *Nanoscale Adv.* **2025,** *7,* 7061–7085. doi:10.1039/d5na00539f
6. Nilghaz, A.; Mahdi Mousavi, S.; Amiri, A.; Tian, J.; Cao, R.; Wang, X. *J. Agric. Food Chem.* **2022,** *70,* 5463–5476. doi:10.1021/acs.jafc.2c00089
7. Chisanga, M.; Muhamadali, H.; Ellis, D. I.; Goodacre, R. *Appl. Sci.* **2019,** *9,* 1163. doi:10.3390/app9061163
8. Muehlethaler, C.; Leona, M.; Lombardi, J. R. *Anal. Chem. (Washington, DC, U. S.)* **2016,** *88,* 152–169. doi:10.1021/acs.analchem.5b04131
9. Yang, Y.; Wu, S.; Chen, Y.; Ju, H. *Chem. Sci.* **2023,** *14,* 12869–12882. doi:10.1039/d3sc04650h
10. Liu, K.-K.; Tadepalli, S.; Tian, L.; Singamaneni, S. *Chem. Mater.* **2015,** *27,* 5261–5270. doi:10.1021/acs.chemmater.5b01401
11. Liu, A.; Gao, C.; Xue, J.; Xie, Y.; Miao, X.; Chen, T.; Wu, A.; Lin, J. *J. Mater. Chem. B* **2026,** *14,* 3071–3092. doi:10.1039/d5tb02751a
12. Li, Q.; Lu, B.; Zhang, L.; Lu, C. *J. Mater. Chem.* **2012,** *22,* 13564–13570. doi:10.1039/c2jm31528a
13. Xia, K.; Yatabe, T.; Yonesato, K.; Kikkawa, S.; Yamazoe, S.; Nakata, A.; Ishikawa, R.; Shibata, N.; Ikuhara, Y.; Yamaguchi, K.; Suzuki, K. *Nat. Commun.* **2024,** *15,* 851. doi:10.1038/s41467-024-45066-9
14. Dreaden, E. C.; Alkilany, A. M.; Huang, X.; Murphy, C. J.; El-Sayed, M. A. *Chem. Soc. Rev.* **2012,** *41,* 2740–2779. doi:10.1039/c1cs15237h
15. Grzelczak, M.; Pérez-Juste, J.; Mulvaney, P.; Liz-Marzán, L. M. *Chem. Soc. Rev.* **2008,** *37,* 1783–1791. doi:10.1039/b711490g
16. Tian, Y.; Cui, Q.; Ma, H.; Jiao, A.; Wang, C.; Zhang, M.; Zheng, L.; Wang, X.; Li, S.; Li, G.; Chen, M. *Appl. Surf. Sci.* **2022,** *578,* 152100. doi:10.1016/j.apsusc.2021.152100
17. Kou, X.; Ni, W.; Tsung, C.-K.; Chan, K.; Lin, H.-Q.; Stucky, G. D.; Wang, J. *Small* **2007,** *3,* 2103–2113. doi:10.1002/smll.200700379

18. Abdul-Moqueet, M. M.; Tovias, L.; Lopez, P.; Mayer, K. M. *Nanotechnology* **2021,** *32,* 225601. doi:10.1088/1361-6528/abe823
19. Chow, T. H.; Li, N.; Bai, X.; Zhuo, X.; Shao, L.; Wang, J. *Acc. Chem. Res.* **2019,** *52,* 2136–2146. doi:10.1021/acs.accounts.9b00230
20. Ye, Z.; Jia, X.; Lou, M.; Huang, H.; Lu, P.; Ye, G.; Gong, X.; Zhu, Y.; Yan, B. *Microfluid. Nanofluid.* **2022,** *26,* 28. doi:10.1007/s10404-022-02535-1
21. Lv, J.; Sun, X.; Zhan, Q.; He, S.; Forsberg, E. *Mater. Res. Express* **2020,** *7,* 025029. doi:10.1088/2053-1591/ab726b
22. Fang, C.; Zhao, G.; Xiao, Y.; Zhao, J.; Zhang, Z.; Geng, B. *Sci. Rep.* **2016,** *6,* 36706. doi:10.1038/srep36706
23. Liu, M.; Guyot-Sionnest, P. *J. Phys. Chem. B* **2005,** *109,* 22192–22200. doi:10.1021/jp054808n
24. Li, Q.; Zhuo, X.; Li, S.; Ruan, Q.; Xu, Q.-H.; Wang, J. *Adv. Opt. Mater.* **2015,** *3,* 801–812. doi:10.1002/adom.201400505
25. Sánchez-Iglesias, A.; Winckelmans, N.; Altantzis, T.; Bals, S.; Grzelczak, M.; Liz-Marzán, L. M. *J. Am. Chem. Soc.* **2017,** *139,* 107–110. doi:10.1021/jacs.6b12143
26. Nguyen, A. L.; Griffin, Q. J.; Wang, A.; Zou, S.; Jing, H. *J. Phys. Chem. C* **2025,** *129,* 4303–4312. doi:10.1021/acs.jpcc.4c08818
27. Srivastava, S.; Sinha, R.; Roy, D. *Aquat. Toxicol.* **2004,** *66,* 319–329. doi:10.1016/j.aquatox.2003.09.008
28. Alderman, D. J. *J. Fish Dis.* **1985,** *8,* 289–298. doi:10.1111/j.1365-2761.1985.tb00945.x
29. National Toxicology Program. TR-527: NTP Technical Report on the Toxicology and Carcinogenesis Studies of Malachite Green Chloride and Leucomalachite Green. 2005; https://ntp.niehs.nih.gov/go/tr527 (accessed Nov 23, 2026).
30. EFSA Panel on Contaminants in the Food Chain (CONTAM). *EFSA J.* **2016,** *14,* e04530. doi:10.2903/j.efsa.2016.4530
31. Ouyang, L.; Yao, L.; Zhou, T.; Zhu, L. *Anal. Chim. Acta* **2018,** *1027,* 83–91. doi:10.1016/j.aca.2018.04.052
32. Bergwerff, A. A.; Scherpenisse, P. *J. Chromatogr., B* **2003,** *788,* 351–359. doi:10.1016/s1570-0232(03)00042-4
33. Zhou, X.; Zhang, J.; Pan, Z.; Li, D. *Anal. Chem. (Washington, DC, U. S.)* **2019,** *49,* 1–20. doi:10.1080/10408347.2018.1456314
34. Johnson, P. B.; Christy, R. W. *Phys. Rev. B* **1972,** *6,* 4370–4379. doi:10.1103/physrevb.6.4370
35. Park, K.; Drummy, L. F.; Wadams, R. C.; Koerner, H.; Nepal, D.; Fabris, L.; Vaia, R. A. *Chem. Mater.* **2013,** *25,* 555–563. doi:10.1021/cm303659q
36. Picciolini, S.; Mehn, D.; Ojea-Jiménez, I.; Gramatica, F.; Morasso, C. *J. Visualized Exp.* **2016,** No. 114, e54319. doi:10.3791/54319
37. Nafisah, S.; Morsin, M.; Sanudin, R.; Nayan, N.; Mohd Yusop, M. Z.; Razali, N. L.; Md Shah, N. Z. A. N. *J. Phys. Chem. Solids* **2021,** *148,* 109764. doi:10.1016/j.jpcs.2020.109764
38. Lee, J.-H.; Gibson, K. J.; Chen, G.; Weizmann, Y. *Nat. Commun.* **2015,** *6,* 7571. doi:10.1038/ncomms8571
39. Agunloye, E.; Panariello, L.; Gavriilidis, A.; Mazzei, L. *Chem. Eng. Sci.* **2018,** *191,* 318–331. doi:10.1016/j.ces.2018.06.046
40. Kumar, S.; Gandhi, K. S.; Kumar, R. *Ind. Eng. Chem. Res.* **2007,** *46,* 3128–3136. doi:10.1021/ie060672j
41. Piella, J.; Bastús, N. G.; Puntes, V. *Chem. Mater.* **2016,** *28,* 1066–1075. doi:10.1021/acs.chemmater.5b04406
42. Deska, R.; Obstarczyk, P.; Matczyszyn, K.; Olesiak-Bańska, J. *J. Phys. Chem. Lett.* **2021,** *12,* 5208–5213. doi:10.1021/acs.jpclett.1c00792
43. Yoo, H.; Jang, M. H. *Nanoscale* **2013,** *5,* 6708–6712. doi:10.1039/c3nr01553j
44. Wong-Ng, W.; McMurdie, H. F.; Hubbard, C. R.; Mighell, A. D. *J. Res. Natl. Inst. Stand. Technol.* **2001,** *106,* 1013–1028. doi:10.6028/jres.106.052
45. Hou, N.; Wen, H.; Chen, W.; Yang, Y.; Jiang, B.; Wang, W.; Huang, S.; Wang, S. *Adv. Colloid Interface Sci.* **2025,** *346,* 103650. doi:10.1016/j.cis.2025.103650
46. Nguyen, Q. N.; Wang, C.; Shang, Y.; Janssen, A.; Xia, Y. *Chem. Rev.* **2023,** *123,* 3693–3760. doi:10.1021/acs.chemrev.2c00468
47. Assad, N.; Laila, M. B.; Hassan, M. N. U.; Rehman, M. F. u.; Ali, L.; Mustaqeem, M.; Ullah, B.; Khan, M. N.; Iqbal, M.; Ercişli, S.; Alarfaj, A. A.; Ansari, M. J.; Malik, T. *Sci. Rep.* **2025,** *15,* 19246. doi:10.1038/s41598-025-02450-9
48. Wang, C.; Singh, P.; Kim, Y. J.; Mathiyalagan, R.; Myagmarjav, D.; Wang, D.; Jin, C.-G.; Yang, D. C. *Artif. Cells, Nanomed., Biotechnol.* **2016,** *44,* 1714–1721. doi:10.3109/21691401.2015.1089253
49. Juodkazis, K.; Juodkazytė, J.; Jasulaitienė, V.; Lukinskas, A.; Šebeka, B. *Electrochem. Commun.* **2000,** *2,* 503–507. doi:10.1016/s1388-2481(00)00069-2
50. Peiris, S.; Sarina, S.; Han, C.; Xiao, Q.; Zhu, H.-Y. *Dalton Trans.* **2017,** *46,* 10665–10672. doi:10.1039/c7dt00418d
51. Oliveira, C.; Chaves, C. R.; Bargiela, P.; da Rocha, M. d. G. C.; da Silva, A. F.; Chubaci, J. F. D.; Boström, M.; Persson, C.; Malta, M. *J. Mater. Res. Technol.* **2021,** *15,* 768–776. doi:10.1016/j.jmrt.2021.08.059
52. Paredes, V.; Manero, J. M.; Salvagni, E. *J. Mater. Sci. Eng.* **2015,** *4,* 193.
53. Cheng, M.; Li, C.; Li, W.; Liu, Y. *Nanomaterials* **2020,** *10,* 1664. doi:10.3390/nano10091664
54. Scarabelli, L.; Sánchez-Iglesias, A.; Pérez-Juste, J.; Liz-Marzán, L. M. *J. Phys. Chem. Lett.* **2015,** *6,* 4270–4279. doi:10.1021/acs.jpclett.5b02123
55. Carone, A.; Emilsson, S.; Mariani, P.; Désert, A.; Parola, S. *Nanoscale Adv.* **2023,** *5,* 2017–2026. doi:10.1039/d2na00809b
56. Kelly, K. L.; Coronado, E.; Zhao, L. L.; Schatz, G. C. *J. Phys. Chem. B* **2003,** *107,* 668–677. doi:10.1021/jp026731y
57. Sammi, H. *Next Res.* **2025,** *2,* 100883. doi:10.1016/j.nexres.2025.100883
58. Radjenovic, P. M.; Zhou, R.-Y.; Dong, J.-C.; Li, J.-F. *J. Phys. Chem. C* **2021,** *125,* 26285–26295. doi:10.1021/acs.jpcc.1c08640
59. Hardy, M.; Chu, H. O. M. *Analyst* **2025,** *150,* 1986–2008. doi:10.1039/d5an00324e
60. Sun, Y.; Zhou, K.; Wang, Y.; Lin, Y.; Wang, W.; Xiong, X.; Zhao, X.; Cui, H.; Liang, M.; Wang, Q.; Yang, S.; Li, L. *Food Chem.* **2025,** *489,* 144920. doi:10.1016/j.foodchem.2025.144920
61. Kumar, P.; Khosla, R.; Soni, M.; Deva, D.; Sharma, S. K. *Sens. Actuators, B* **2017,** *246,* 477–486. doi:10.1016/j.snb.2017.01.202
62. Zhang, W.; Luo, K.; Chen, W.; Chen, M.; Cai, N.; Li, J. *Spectrochim. Acta, Part A* **2026,** *345,* 126813. doi:10.1016/j.saa.2025.126813
63. Qian, X.; Emory, S. R.; Nie, S. *J. Am. Chem. Soc.* **2012,** *134,* 2000–2003. doi:10.1021/ja210992b
64. Li, Z. H.; Bai, J. H.; Zhang, X.; Lv, J. M.; Fan, C. S.; Zhao, Y. M.; Wu, Z. L.; Xu, H. J. *Spectrochim. Acta, Part A* **2020,** *241,* 118532. doi:10.1016/j.saa.2020.118532

License and Terms

This is an open access article licensed under the terms of the Beilstein-Institut Open Access License Agreement (https://www.beilstein-journals.org/bjnano/terms), which is identical to the Creative Commons Attribution 4.0 International License (https://creativecommons.org/licenses/by/4.0). The reuse of material under this license requires that the author(s), source and license are credited. Third-party material in this article could be subject to other licenses (typically indicated in the credit line), and in this case, users are required to obtain permission from the license holder to reuse the material.

The definitive version of this article is the electronic one which can be found at:
https://doi.org/10.3762/bjnano.17.115